Small-Signal Equivalent Circuit Model as a Tool for Optimizing Millimeter-Wave Detection With FETs

Gaudencio Paz-Martínez, Ignacio Íñiguez-De-La-Torre, Philippe Artillan, Edouard Rochefeuille, Sergio García-Sánchez, Tomás González, Javier Mateos

Small-Signal Equivalent Circuit Model as a Tool for Optimizing Millimeter-Wave Detection with FETs

Gaudencio Paz-Martínez, Ignacio Íñiguez-de-la-Torre, Philippe Artillan, Edouard Rochefeuille, Sergio García-Sánchez, Tomás González, *Senior Member, IEEE,* and Javier Mateos, *Member, IEEE*

***Abstract*—The responsivity of sub-THz zero-bias detectors based on GaN high electron mobility transistors (HEMTs) is measured up to 110 GHz. A predictive model based on static coefficients extracted from the dc output curves together with S-parameter measurements is able to replicate the detection results both when the radio-frequency power is fed into the drain or the gate terminals. The gate-drain coupling, counteracting the contribution of the direct modulation of the drain voltage to the RF responsivity, is at the origin of the frequency roll-off of the detection, and therefore, the frequency performance is improved when shrinking the gate size of the transistors. The extraction of the small-equivalent circuit allows understanding the influence of the parasitic elements and the scaling of the gate width of the transistors on the detection performance, as well as extrapolating the results of the measurements to predict the performances at higher frequencies. In addition, the analysis of the influence of the different equivalent-circuit elements allows linking the values of the responsivity and noise equivalent power to the physics of the transistor operation and thus determining at which frequency the detection roll-off appears as a function of the gate length and width, and confirming that both must be reduced as much as possible in order to optimize the transistor high-frequency operation, the latter having a more significant influence.**

***Index Terms*—GaN high electron mobility transistors (HEMTs), Sub-THz detection, Small Signal Equivalent-circuit, Zero-bias detector**

I. Introduction

In addition to the well-known and commercially accessible Schottky barrier diodes [1], THz detectors based on different technologies (bolometers, pyroelectric detectors, Golay cells, Josephson junctions or resonant tunneling diodes) are presently available [2], [3], [4]. In recent years, Field Effect Transistors (FETs) have also started to be used as sensitive RF detectors up to frequencies above their cutoff for their classic amplification function. Plasma effects are often claimed to be the physical origin of the THz detection with FETs [5], [6], [7] (thus typically called "plasma detectors"), even if a photothermoelectric effect process can also have a significant contribution [8], [9]. However, at lower frequencies, in the millimeter-wave range, FETs operate through the resistive self-mixing mechanism, in which the RF signal injected into the gate or drain terminals provides a non-zero dc current (or voltage) due to the device non-linearity. An external gate-drain capacitance is often added to the transistor in the case of gate injection to enhance the coupling of the signal to the drain port and allow for RF detection at low frequencies [10], [11].

Several circuit-based models have been used for the modeling of RF power detection with FETs, from a classical lumped element equivalent circuit point of view [10], [12], to a distributed resistive self-mixing model [13], [14], [15] which extends the validity of the equivalent circuit description to frequencies above their cutoff. Such models have been able to provide a good description of the FET responsivity over a wide bandwidth, reaching the THz range [11]. However, they only provide a qualitative description of the detection mechanism, as they usually only consider the intrinsic part of the transistors (typically just the region below the gate), and few works take into account the real geometry of the transistors and the inevitable presence of parasitic elements (resistances, capacitances and inductances) associated with the contacts and accesses to the device terminals [12], [16]. In this paper we propose the use of a complete Small-Signal Equivalent Circuit (SSEC) description of the transistors employing the standard model for FETs [17], [18], [19], [20], able to precisely describe their frequency response (represented by their experimental S-parameter matrix). We will also take advantage of the closed-form expression (CFE) for the current responsivity developed in our recent paper [21], which, taking as a base the experimental measurements of the I-V curves and the frequency-dependent S-parameters of any transistor, is able to analytically provide the value of its detection responsivity in both gate or drain injection conditions. The only intent to use a similar practical SSEC description of FETs, also linked to a closed-form expression of the responsivity, was made by Khan et al. in Ref. [22], employing a similar approach to that proposed here. However, as explained in our previous work [21], the closed-form expression used in [22] is not completely correct, as it does not adequately take into account the reflected voltage wave (due to the impedance mismatch) at the input, which we include here in terms of the S-parameters of the transistor. Andersson $etal.$ [10] use the measured S-parameters to extract the elements of the SSEC and together with the I-V curves to extend the analytical description of the detector response to the high-frequency regime by making assumptions which are valid only in specific frequency ranges. In our case,

Manuscript received XX Month 2023. This work has been partially supported through Grant PID2020-115842RB-I00 funded by MCIN/AEI/10.13039/501100011033 and the Junta de Castilla y León and FEDER through project SA136P23. *(Corresponding author: Gaudencio Paz-Martínez)*

G. Paz-Martínez, I. Íñiguez-de-la-Torre, S. García-Sánchez, T. González and J. Mateos are with with the Applied Physics Department, and USAL-NANOLAB, Universidad de Salamanca, 37008 Salamanca, Spain (e-mail: gaupaz@usal.es, indy@usal.es, sergio_gs@usal.es, tomasg@usal.es, javierm@usal.es).

P. Artillan and E. Rochefeuille are with Univ. Grenoble Alpes, Univ. Savoie Mont Blanc, CNRS, Grenoble INP, CROMA, 38000 Grenoble, France (e-mail: philippe.artillan@univ-smb.fr, edouard.rochefeuille@univ-smb.fr).

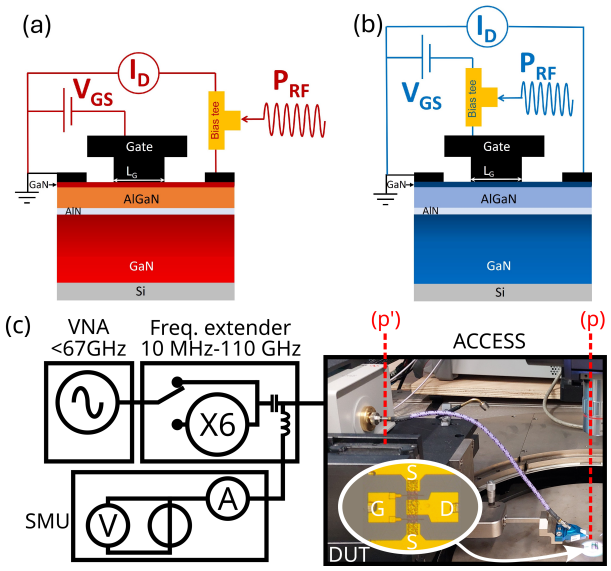

Fig. 1. Schematic drawing of the two configurations used for current detection: (a) RF power injected into the drain (DI) and (b) into the gate (GI). (c) Experimental setup to carry out the GSG (100 μm pitch) on-wafer measurements up to 110 GHz. One channel of the SMU is used both to bias the drain with V_{DS}=0 V and measure the drain current I_D, and the other to apply the gate voltage V_{GS}. The RF power can be injected either in the drain or in the gate port. An internal bias-tee allows us to couple dc and RF signals. The drain current is measured as detection output.

using a similar approach, we cover all the frequency range of interest without the need for any assumption, allowing us to quickly predict the responsivity and thus facilitating the design optimization of FET-based RF power detectors.

The advantage of AlGaN/GaN FETs for the implementation of RF power detectors is that they have a large, dynamic range so that they can be used as high-power detectors, and can operate over a wide range of temperatures [23], [24],while their broadband detection capability has already been demonstrated [12] (even if HEMTs based on high-mobility materials such as InGaAs can provide improved performances [25]). Gaining a deeper insight into the physical origin of the limitations (mainly in frequency) of the detection mechanism is essential for maximizing the performances of FET detectors to their utmost potential. As such, we consider our approach to be quite powerful and also applicable not only to GaN HEMTs but to any kind of FET technology.

In this work, we analyze standard GaN high electron mobility transistors (HEMTs) without adding any external element, which are more suitable for understanding the physics behind the detection process. We study their performance in zero-bias current detection mode (with short-circuited drain) with different gate sizes. Their relationship with the results attained in voltage-detection mode (open circuited drain) was explained in previous works, both above and below threshold [26], [27]. We will use a recently proposed analytical model based on static coefficients obtained from dc measurements which, together with the S-matrix obtained from the RF characterization of the devices, is able to explain the phenomena behind the observed dependencies of the detection experiments up to 67 GHz [21]. Here we extend the verification of the validity of the model with measurements up to 110 GHz (some of them already presented in [28]), and extract a SSEC model of the transistors exploited to interpret the detection results. This is a very noteworthy addition, since the SSEC description of the detectors provides significant benefits: it not only allows drawing conclusions about the influence of the different parameters on the detection performances (and thus optimize the device topology), but also to extrapolate them to frequencies above the experimental limit.

II. Devices Under Test and Experimental Setup

Our devices under test are HEMTs with an AlGaN/GaN heterojunction grown on a high-resistivity Si substrate [29]. The heterostructure has a 14 nm thick AlGaN (29% Al) layer, on a 1.73 μm thick GaN buffer, with a 1 nm AlN spacer in the middle to improve carrier confinement within the 2DEG, and a 0.5 nm thick GaN cap on the top of the heterostructure. The transistors have been passivated with a N_2O pretreatment and a 150 nm layer of SiN. Hall measurements of the wafer have provided a mobility of about 2000 $\mathrm{cm}^2/\mathrm{Vs}$.

The measurements of current responsivity have been performed in two transistors with L_G=75 nm (W=2×25 μm, called T-75) and L_G=250 nm (W=2×50 μm, called T-250), both with L_{DS}=2.5 μm. These transistors, working as classical amplifiers, exhibit cutoff frequencies above 100 GHz when they are biased in saturation. More precisely, T-75 provides f_t=116 GHz and f_{max}=150 GHz [29], while T-250 shows f_t=60 GHz and f_{max}=100 GHz [30]).

The same setup described in [21] and sketched in Fig. 1(c), with the RF source being a VNA, has been employed. A SMU was used to impose the zero-bias condition of null excitation voltage and measure the output current. The RF signal was generated by means of a Keysight N5251A Single Sweep Solution (10 MHz to 110 GHz) Millimeter Wave System, either directly from the internal source of the VNA at base frequency range (up to 67 GHz), or by frequency-multiplying the source with a frequency extender. In order to deliver a precisely known power P at the reference plane of the transistor (p), dedicated on-wafer SOL and power calibration at base range (up to date factory calibration of the setup) and at 75-110 GHz band (thanks to a powermeter with specific probe) have been carried out at the output reference plane of the extender head (p') to determine the losses in the cables and the probes. All measurements have been performed in the dark and at room temperature. A macro code was implemented in MATLAB to automate the control of the instruments and set the actual incident power to P=-20 dBm. The RF signal can be injected into the drain (DI) or the gate (GI) ports of the HEMTs, see Fig. 1, while the detected dc current response in both schemes is measured and averaged at the (short-circuited) drain terminal. Here we focus intentionally in zero-voltage bias detection, V_{DS}=0 V, in order to minimize the output noise and improve the sensitivity. The responsivity is obtained as the ratio $\beta = \frac{\Delta I_D}{P}$, where ΔI_D is the dc shift of I_D caused by the RF excitation and a subscript d or g is added to distinguish between DI and GI schemes (β_d and β_g).

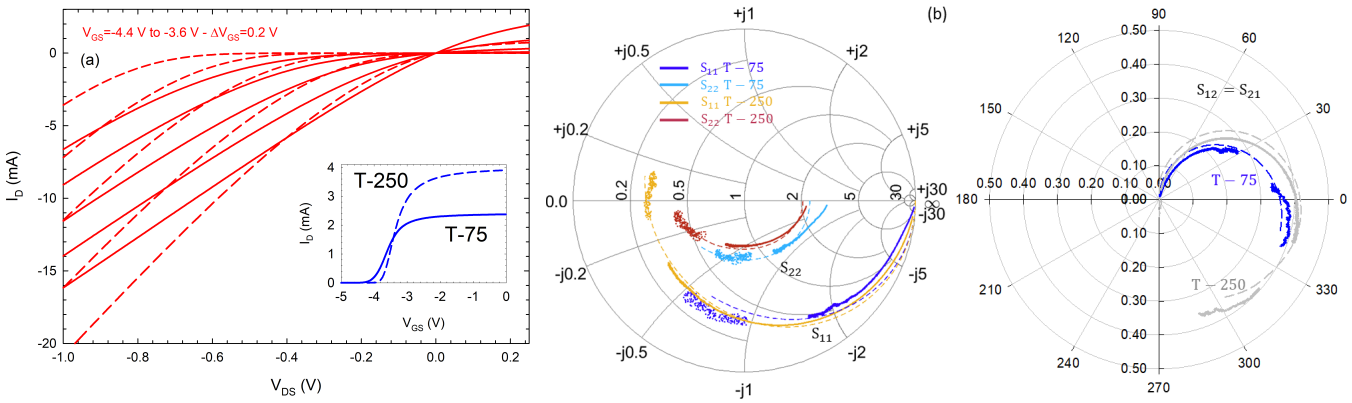

Fig. 2. (a) Output I_D-V_{DS} curves for T-75 (solid) and T-250 (dashed) transistors. The inset shows the transfer curve measured at V_{DS}=0.1 V. S-parameters for V_{DS}=0 V and V_{GS}=-3.8 V (T-75) and V_{GS}=-3.3 V (T-250) are presented in (b): S_{11} and S_{22} in Smith chart format, and S_{12}=S_{21} (as for V_{DS}=0 the transistor acts as a passive element) in polar format. Experimental results are plotted with dots, and with dashed lines the results of the SSEC model.

III. Results and Discussion

A. DC Curves and S-parameters

The ingredients for our model are (i) the non-linearity of the transistor, accounted for by the measured dc curves, and (ii) its frequency dependent behavior, described by the S-parameter data, both shown in Fig. 2 for the HEMTs under study. In (b), the S-parameters of the transistors are shown at the bias point for maximum responsivity, V_{GS}=-3.8 V (as usual, the drain is connected to port 2 of the VNA while the gate corresponds to port 1). Fig. 2(a) shows that both T-75 and T-250 have a similar threshold voltage, V_{th}, of around -4 V (slightly higher for T-75), and also that the drain conductance around V_{DS}=0 is larger in T-75 than in T-250. This fact leads, regarding the S-parameters of the devices, to a much higher value of S_{22} in T-250, Fig 2(b), due to a stronger impedance mismatch with the 50 Ω line. Typically GaN HEMTs display low-frequency dispersion effects due to traps [31], this could be the origin of the discrepancies between the simulated and measured data of S-parameters in Fig 2(b).

B. Current Responsivity for Different Gate Sizes

Fig. 3(a) shows the typical bell shape dependence of β_d *vs.* V_{GS} measured in the T-75 HEMT, showing a maximum (in absolute value, since it is negative) for a gate bias slightly above the threshold voltage. β_d is almost frequency independent below 20 GHz, but decreases at high frequency, being almost halved at 60 GHz. Moreover, the inset shows a practically ideal square law response at 1 GHz, with a large dynamic range of more than 30 dB. The results obtained in transistors with different gate lengths are similar, as shown in Fig. 3(b), with just a V_{GS} shift due to the increase of V_{th} (more negative for shorter L_G due to short-channel effects). The inset of Fig. 3(b) shows that, as expected, β_d is proportional to W and almost independent of L_G [25] at low frequencies.

The measured frequency dependence of β_d and β_g (both for T-75 and T-250) is plotted in symbols in Fig. 4 for the V_{GS} value where the maximum responsivity occurs for each transistor. Note the different sign of each responsivity,

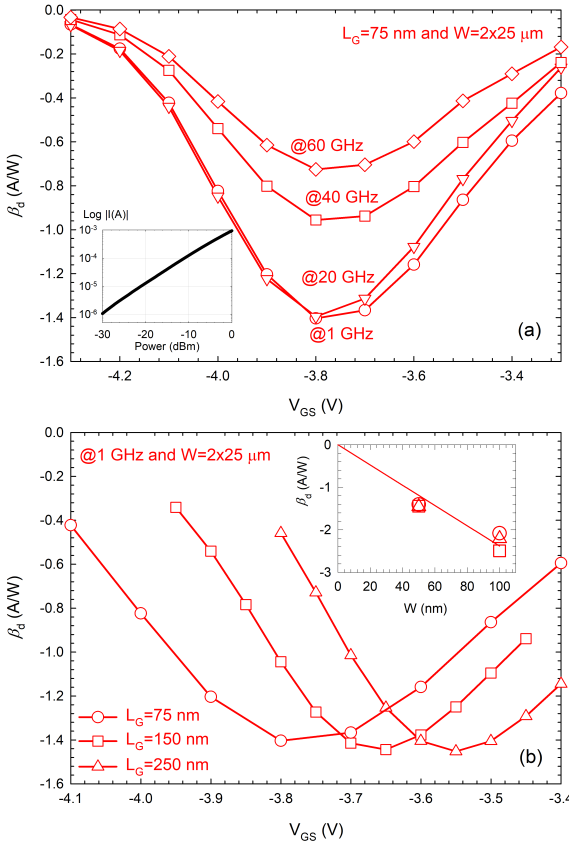

Fig. 3. Current responsivity β_d in A/W as a function of V_{GS} measured in (a) the transistor T-75 (L_G=75 nm and W=2×25μm) for different values of the frequency of the injected RF signal (with -20 dBm power) and (b) transistors with L_G=75, 150 and 250 nm with W=2×25μm at 1 GHz. The inset in (a) shows the output current *vs.* input RF power (at 1 GHz frequency), showing a quasi-ideal square law response and that in (b) the peak value of β_d *vs.* W for the three values of L_G.

being β_d negative while β_g is positive. The frequency roll-off, studied in more detail later, of β_d, typically characterized by the -3 dB frequency (f_{3dB}, corresponding to a halved responsivity), appears at higher frequencies with the reduction of both L_G and W due to the smaller gate capacitance (being specifically C_{gd} the key parameter). Indeed, f_{3dB} increases

from about 20 GHz for T-250 to about 30 GHz for the HEMT with half W (L_G=250 nm W=2×25 μm, not shown here), and to 50 GHz for T-75. This happens because the drain-gate coupling, which has a positive contribution to the current detection (opposite to the negative one associated to the direct drain rectification [10], the only one appearing at low frequency in β_d) is practically proportional to C_{gd}.

It is this fact which makes more complex the frequency behaviour of the responsivity for the GI configuration, β_g. It is null at low frequency, since a drain-gate coupling is needed for having a non-zero value of I_D for V_{DS}=0 V. In absence of an external C_{gd} capacitor, the increase of β_g coincides with the frequency roll-off of the transistor detection in the DI configuration, so that no plateau is observed in the β_g *vs.* f behaviour, Fig. 4(b).

In [21] we have proposed a generic high frequency model of two-port RF detectors where a closed-form expression, based on (i) the static coefficients defined as g_{ij}=$\partial^{(i+j)}I_D/\partial^i V_{GS}\partial^j V_{DS}$ extracted from the I_D-V_{DS} curves and (ii) the measured the S-parameters, is able to replicate both responsivities, particularized in the following equations:

$$\beta_d=\frac{R_0}{2}(\underbrace{g_{20}\,|S_{12}|^2}_{\beta_{d,20}}+\underbrace{g_{02}\,|1+S_{22}|^2}_{\beta_{d,02}}+\underbrace{2g_{11}\Re[S_{12}^*(1+S_{22})]}_{\beta_{d,11}}), \quad (1)$$

$$\beta_g=\frac{R_0}{2}(\underbrace{g_{20}\,|1+S_{11}|^2}_{\beta_{g,20}}+\underbrace{g_{02}\,|S_{21}|^2}_{\beta_{g,02}}+\underbrace{2g_{11}\Re[S_{21}^*(1+S_{11})]}_{\beta_{g,11}}), \quad (2)$$

where R_0=50 Ω is the typical output impedance of the source. The results of the model (solid lines in Fig. 4), which accurately reproduce the DI and GI detection experiments in all the frequency span (symbols), will be used to explain the observed dependencies on the gate length and width.

C. Contributions to the Responsivity

The contributions of each term of eqs. (1) and (2), indicated in curly brackets, are plotted in Fig. 5; the one proportional to g_{02} (β_{02}) representing the direct drain detection, and that on g_{11} (β_{11}) associated to the gate-drain coupling. Note that for a zero-bias detector the term proportional to g_{20} (β_{20}) is null (g_{20}=g_m=0 for V_{DS}=0, since a non-null drain voltage is needed for having drain current). It is now clear that the frequency roll-off of the RF detection within the DI configuration is mainly due to the contribution of the gate-drain coupling (opposite to the direct drain detection), which appears at higher frequencies as C_{gd} is reduced. Conversely, in the case of the GI configuration, the increase of β_g, also linked to that same mechanism, follows a similar trend with frequency.

Fig. 6 shows the estimated noise equivalent power (NEP) calculated with the expression [24]:

$$NEP=\frac{\sqrt{4k_BT/R_{DS}}}{\beta}, \quad (3)$$

where R_D is the drain resistance at V_{DS}=0, k_B is Boltzmann's constant, T is the lattice temperature and β is the measured current responsivity (in DI or GI conditions). The optimum

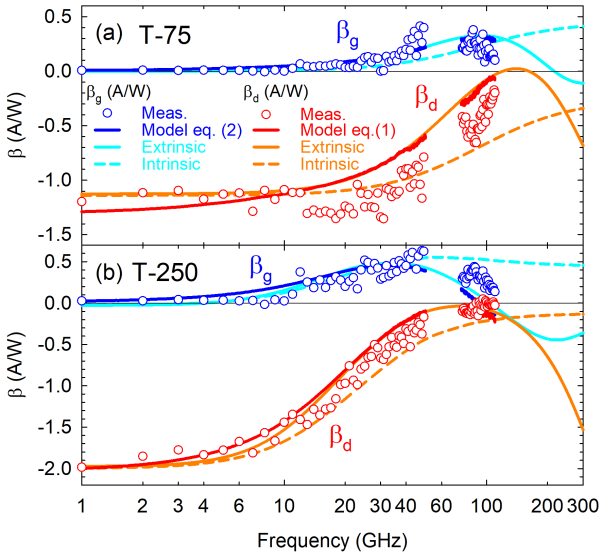

Fig. 4. Measurements (symbols) of β_d and β_g compared to the results of the closed-form expression given by eqs. (1) and (2), respectively, as a function of the excitation frequency for the two HEMTs under study (a) T-75 and (b) T-250. The results of the closed-form expressions obtained using the experimental S-parameters are compared with those provided by the SSEC model with and without considering the parasitic elements.

NEP is obtained at low frequency in DI configuration for the device with the largest gate, as expected due to the higher value of the measured β_d observed in Fig. 4 This remains the case until around 13 GHz, where the behavior changes and at higher frequencies the device with the shortest gate is the one with the best NEP compared to the longest one, due to a better frequency response. In the case of GI, the NEP at low frequencies is very high, but as around 11 GHz β_g begins to increase, the NEP decreases until reaching his optimal value at the frequency where β_g reaches the maximum; after this point it increases again due to a lower responsivity.

D. Small-Signal Equivalent Circuit Analysis

For a better understanding of the response of transistors with different gate sizes, we use the SSEC shown in Fig. 7. The yellow box includes the intrinsic elements, and the extrinsic elements are outside of it. This circuit is similar to that presented by Malmkvist *et al.* [32], adding the C_{gd}^{ext}, C_{gs}^{ext} and C_{ds}^{ext} elements of the equivalent circuit proposed by Mateos *et al.* [18] to account for parasitic capacitances which are not associated to the access regions and are not typically included in the extrinsic parameters obtained by means of RF measurements of dummy structures. As a first approximation we use Dambrine's method [17] to determine the approximate value of the lumped elements of the yellow region of Fig, 7. Once this step is done, three extrinsic capacitance's (blue box) and the R_{gd} resistance are included in Quite Universal Circuit Simulator (QUCS) to do a fine-tuning of the values of the circuit elements by comparing the measured (10 MHz-110 GHz) and simulated S-parameters. As shown in Fig. 2 a good agreement is obtained between the experimental values and those obtained from the SSEC model.

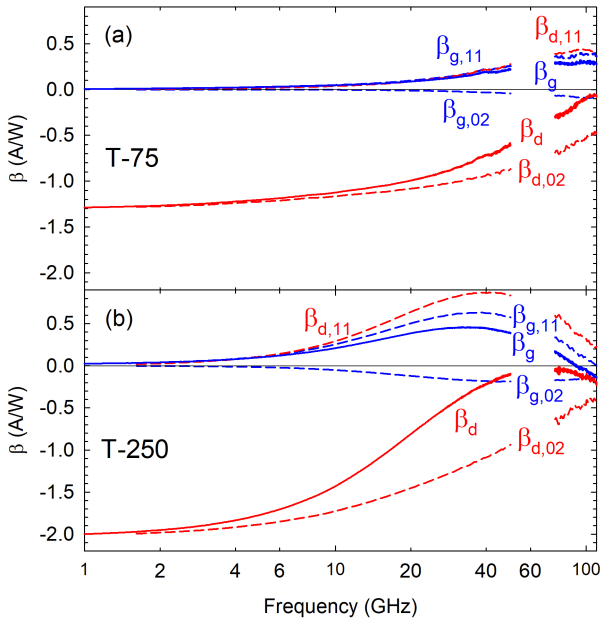

Fig. 5. Contribution of each term of 1 and 2 to the responsivities β_d and β_g calculated with the measured S-Parameters up to 110 GHz for (a) T-75 and (b) T-250

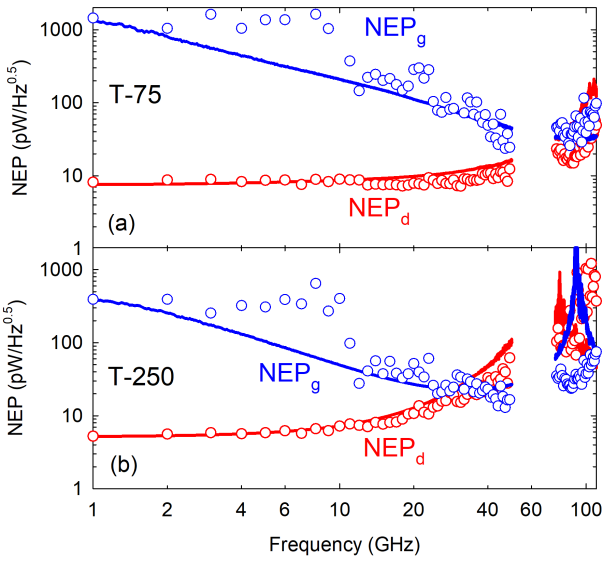

Fig. 6. NEP $vs.$ frequency at equilibrium calculated with eq. (3) for (a) T-75 and (b) T-250.

Once the circuit elements have been optimized, the simulated S-parameters are extrapolated to frequencies higher than 110 GHz, at which we can predict the detector behavior with the closed-form expressions for the responsivity. Another advantage of the S-parameters thus simulated is that the response of the circuit can be initially predicted with just the intrinsic elements and then also including the extrinsic ones, thus allowing to identify their respective effects on the responsivity. The optimized values of the elements of the SSEC are presented in Table I at the bias point of the optimum responsivity analyzed in Fig. 4.

Fig. 4 shows the responsivity calculated (by means of the

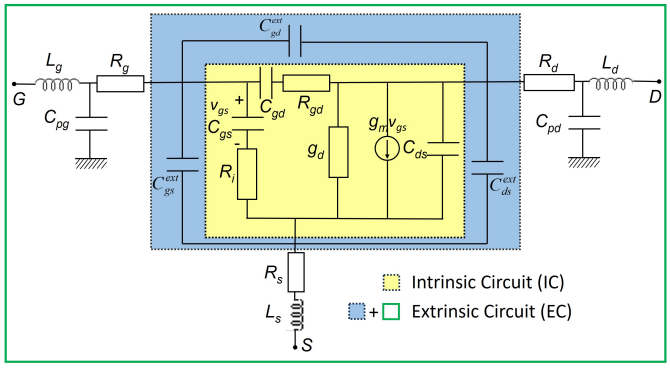

Fig. 7. SSEC used for the HEMTs. Note that for V_{DS}=0 g_m is null.The yellow box corresponds to the intrinsic circuit (IC), the blue and white one to the extrinsic circuit (EC).

TABLE I
VALUES OF THE ELEMENTS OF THE SSEC FOR THE BIAS POINT WITH OPTIMUM RESPONSIVITY (V_{GS}=-3.8 V FOR T-75 AND V_{GS}=-3.3 V FOR T-250). THE EXTRINSIC ELEMENTS ARE TAKEN TO BE CONSTANT, WITH R_g=R_d=R_s=1 Ω.

Intrinsic elements	T-75	T-250
C_{gd} (fF/mm)	195	500
C_{gs} (fF/mm)	155	340
C_{ds} (fF/mm)	2.0	2.0
R_{gd} (Ω×mm)	4.5	3.4
R_i (Ω×mm)	13.0	5.0
g_d (mS/mm)	181	100

Extrinsic elements	T-75	T-250
L_g (pH)	20	33
L_d (pH)	25	27
L_s (pH)	10	5
C_{pg} (fF)	8	15
C_{pd} (fF)	11	15
C_{gd}^{ext} (fF)	7.55	15
C_{gs}^{ext} (fF)	5.9	15.5
C_{ds}^{ext} (fF)	7.0	2.0

closed-form expressions) with the S-parameters provided by the intrinsic (dashed lines) and extrinsic (continuous line) SSECs with data extrapolated up to 300 GHz, compared with that calculated with the S-parameters measured up to 110 GHz. With the intrinsic SSEC (IC) in DI configuration, β_d is flat at low frequencies, but when the frequency increases the response decreases and tends to zero. In the case of the extrinsic SSEC (EC), β_d follows the same trend (with the decay starting at lower frequencies), but, interestingly, after reaching a minimum value, it increases at the highest frequencies. This is due to the fact that the term $\beta_{d,11}$ changes sign and adds up to the also negative contribution of $\beta_{d,02}$. Indeed, at high frequencies, the parasitic elements act as a complex network (not just a short-circuiting capacitor between gate and drain) which applies a signal to the gate terminal with opposite phase to that injected in the drain, thus enhancing the total response. In GI configuration, for IC, due to the effect of C_{gd}, β_g is null at low frequencies but increases with increasing frequency, reaching a maximum flat response. By contrast, β_g for EC reaches a maximum value and then decreases again due to the complex gate-drain coupling induced by the parasitic elements of the SSEC.

These effects can be better understood if, alternatively,

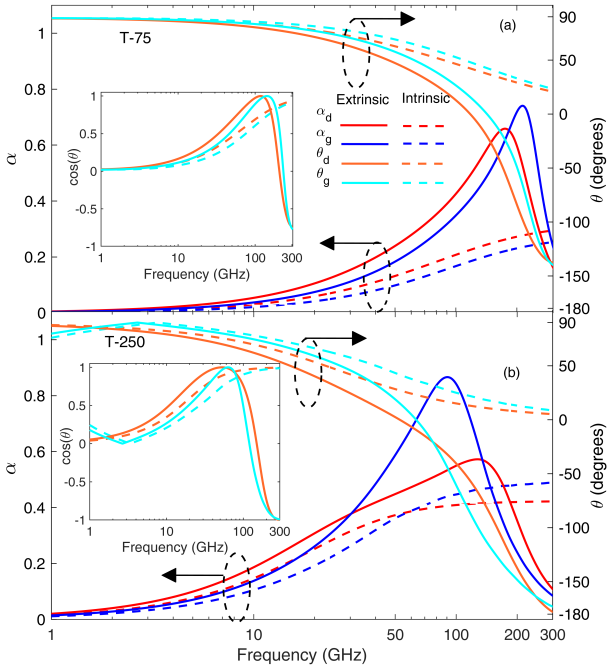

Fig. 8. Comparison between intrinsic (dashed lines) and extrinsic (continuous lines) coupling factor α and phase difference between gate and drain voltages θ, in both DI and GI cases, for devices (a) T-75 and (b) T-250. The values of cos(θ) are shown in the insets.

equations 1 and 2 are written as

$$\beta_d = \frac{R_0}{2}\left(\underbrace{\alpha_d^2 g_{20}}_{\beta_{d,20}} + \underbrace{g_{02}}_{\beta_{d,02}} + \underbrace{\alpha_d 2 g_{11}\cos\theta_d}_{\beta_{d,11}}\right)|1+S_{22}|^2, \quad (4)$$

$$\beta_g = \frac{R_0}{2}\left(\underbrace{g_{20}}_{\beta_{g,20}} + \underbrace{\alpha_g^2 g_{02}}_{\beta_{g,02}} + \underbrace{\alpha_g 2 g_{11}\cos\theta_g}_{\beta_{g,11}}\right)|1+S_{11}|^2, \quad (5)$$

where α_d=v_{gs}/v_{ds} and α_g=v_{ds}/v_{gs} represent the RF amplitude ratios of v_{gs} with respect to v_{ds} and of v_{ds} with respect to v_{gs}, respectively. These parameters are a measure of the coupling of the RF signal between ports. θ_d and θ_g are the phase differences between the injected signal (v_{ds} in DI and v_{gs} in GI) and the coupled signal (v_{gs} in DI and v_{ds} in GI).

Figs. 8(a) and (b) show in the left y-axis the coupling ratios α_d and α_g obtained with the IC (dashed line) and the EC (continuous line) S-parameters. The phase between the injected and coupled signal (θ_d and θ_g) for the IC (dashed line) and EC (continuous line) cases are shown in the right y-axis of Fig. 8. While DI and GI schemes provide similar results, clear differences are observed between the IC and EC cases. In the IC case, the values of α are null at low frequencies and then increase with frequency up to a constant value, while in the EC calculation they reach a maximum at a given value of frequency (lower for the longer gate) and then decrease. Regarding the phase differences, θ, in the IC case it changes from 90 degrees at low frequency to around 20 degrees at 300 GHz (as expected from a capacitive coupling, i.e. a high-pass filter), but in the EC case, θ changes from 90 degrees at low frequency to around -170 degrees at 300 GHz due to the significant influence the inductive extrinsic elements of the SSEC have at high frequency. Remarkably, this evolution of θ

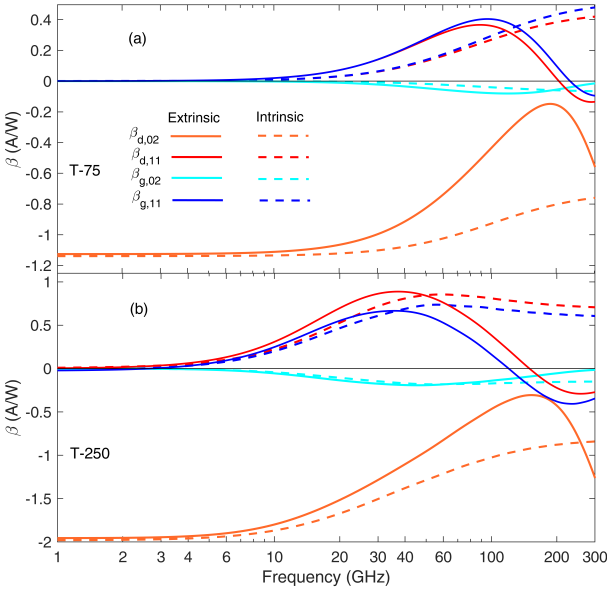

Fig. 9. Contribution of $\beta_{d,11}$, $\beta_{g,11}$, $\beta_{d,20}$ and $\beta_{g,20}$ of 4 and 5 in EC and IC for (a) T-75 and (b) T-250.

provokes a sign change of cos(θ) when θ goes below zero, see inset of Fig. 8, thus making the contribution of the β_{11} term to add up to that of β_{02} instead of counteracting it (the gate-drain-coupling increases the total responsivity in that case).

This behavior of θ is at the origin of the differences found between the responsivity in both DI and GI configurations between the IC and the EC at high frequencies. The terms $\beta_{d,11}$ and $\beta_{g,11}$ in 4 and 5 for the IC and shown in Fig. 9 with dashed lines tend to a maximum constant value (as θ goes to zero), thus dominating over $\beta_{d,02}$ and $\beta_{g,02}$, which starts a frequency roll-off at that same frequency range. In the EC case $\beta_{d,11}$ and $\beta_{g,11}$ reach a maximum value when θ is zero, so that the total β_g reach their maximum at around 100 GHz for T-75 and 50 GHz for T-250, see Figs. 4(a) and (b). Then, when θ goes to negative values, see Figs. 9(a) and (b), $\beta_{d,11}$, $\beta_{g,11}$, $\beta_{d,20}$ and $\beta_{g,20}$ have all negative sign, so that β_g becomes negative and β_d surprisingly starts to grow up after decreasing to almost zero.

E. Analysis of f_{3dB} frequency in drain injection using the SSEC

For comparison purposes, in DI the value of the simulated β_d is normalized to its value at 1 GHz, and the result is shown in Fig. 10. As expected, the shortest device (T-75) exhibits the highest value of f_{3dB}=50 GHz for the EC case (126 GHz for the IC), while for T-250 f_{3dB} decreases to 17 GHz (24 GHz in the IC case). The analysis of the SSEC model shows that the elements that mostly affect this parameter in the case of the IC are C_{gd} and g_d, while in the EC the extrinsic elements have a very important additional influence on reducing the responsivity. As shown in Fig. 8, θ in the IC case has a behavior similar to a high-pass filter (as a consequence a purely capacitive coupling between gate and drain), but for the EC the phase it resembles that of a band-pass filter (due to the addition of the parasitic inductances). It should be noted that

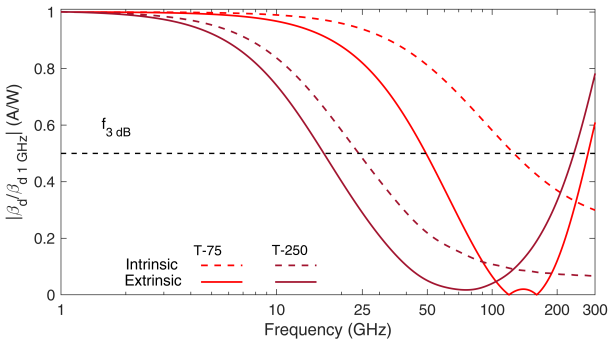

Fig. 10. Normalized value of β_d up to 200 GHz for IC (dashed line) and EC (continuous line), the horizontal dashed black line represents the value for which the responsivity falls to 50% and f_{3dB} is taken.

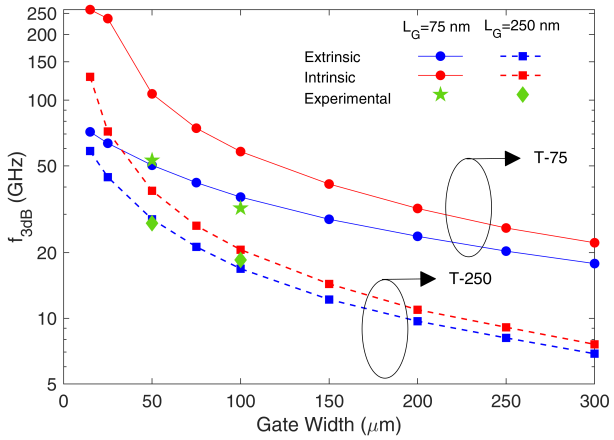

Fig. 11. Comparison of modeled and experimental values obtained for f_{3dB} in DI as a function of the gate width, W, for devices with L_G=75 nm and L_G=250 nm. The values obtained with the models of extrinsic (blue lines and symbols) and intrinsic (red lines and symbols) SSEC elements are shown.

f_{3dB} is lower than the expected cutoff frequency of the device, mainly due to the competition between the contributions of the β_{11} and β_{20} terms, with the circuit elements associated to the pads also playing a important role in the frequency roll-off.

Exploiting the powerful capabilities of the SSEC model, we study the influence of the gate width on the frequency behaviour of the detection with DI. For that sake, the values of the intrinsic elements of the SSEC have been appropriately scaled (capacitances and conductances are proportional to W, and the parasitic elements are kept constant) and the S-parameters as a function of W have been computed using QUCS. The intrinsic and extrinsic responsivities are then calculated using eqs. (1) and (2). The values obtained for f_{3dB} are shown in Fig. 11 for both T-75 and T-250. It shows how, first, the experimental values of the devices with different values of W (L_G=75 nm with W=100 μm and L_G=250 nm W=50μm) are precisely reproduced by the model. On the other hand, as expected, it is observed that the shorter the gate the higher the detection bandwidth is, but as the gate width is shortened f_{3dB} increases and the influence of L_G decreases. This is due to the significant effect of the parasitics, which counteracts the expected improvement obtained with the reduction of the gate length. As a consequence, the optimum design for an improved f_{3dB} is to reduce as much as possible both the gate width and the parasitics.

Finally, we remark that non-quasi static (NQS) effects are not accounted for in the SSEC model presented in this work, and neither in the used closed-form expressions, where the non-linearity coefficients g_{ij}, are considered to be frequency independent. To include NQS effects (which appear at much higher frequencies than those studied here), complex frequency dependent g_{ij} coefficients should be used. Other possibility is to use complex NQS SSEC models, as that derived from drift-diffusion calculations in [33], but the study of such sophisticated models fall outside the objective of this work.

IV. Conclusions

We have analyzed the differences exhibited by GaN HEMTs with different gate sizes when operating as zero-bias sub-THz power detectors by means of measurements up to 110 GHz and simulations based on the SSEC up to 300 GHz in two schemes, DI and GI. A robust model is able to replicate the frequency dependence of the experiments and explain its physical origin with the help of simulated S-parameters. The decrease in the DI responsivity coincides with the increase of the GI one, due to the capacitive gate-drain coupling. We demonstrate that the high frequency roll-off of the detection can be optimized with the reduction of both L_G and W due to the smaller gate-drain capacitance. The circuit elements that degrade the frequency response are principally C_{gd}, the drain conductance g_d and the parasitic elements associated with the pads. Finally, the SSEC model allows studying the influence of the gate width scaling on the frequency behaciour of the DI detection, showing that high-frequency operation is significantly benefited by reducing W. On the other hand, shortening the gate length is not so much effective for small W, as the effect of the parasitics counteracts the improvement of the intrinsic behavior.

References

[1] J. L. Hesler and T. W. Crowe, "NEP and responsivity of THz zero-bias Schottky diode detectors," in *2007 Joint 32nd Int. conf. on infrared and mm waves and the 15th Int. conf. on THz electronics*, 2007, pp. 844–845.
[2] F. Sizov and A. Rogalski, "THz detectors," *Progress in Quantum Electronics*, vol. 34, no. 5, pp. 278–347, 2010.
[3] F. Aniel *et al.*, *Terahertz electronic devices*. Springer, 2022.
[4] E. Javadi, D. B. But, K. Ikamas, J. Zdanevičius, W. Knap, and A. Lisauskas, "Sensitivity of field-effect transistor-based terahertz detectors," *Sensors*, vol. 21, no. 9, p. 2909, 2021.
[5] M. Dyakonov and M. Shur, "Detection, mixing, and frequency multiplication of terahertz radiation by two-dimensional electronic fluid," *IEEE Trans. Electron Devices,*, vol. 43, no. 3, pp. 380–387, 1996.
[6] S. Boubanga-Tombet *et al.*, "Current driven resonant plasma wave detection of terahertz radiation:: Toward the dyakonov-shur instability," *Appl. Phys. Lett.*, vol. 92, no. 21, 2008.
[7] M. Sakowicz, M. Lifshits, O. Klimenko, F. Schuster, D. Coquillat, F. Teppe, and W. Knap, "Terahertz responsivity of field effect transistors versus their static channel conductivity and loading effects," *J. Appl. Phys.*, vol. 110, no. 5, p. 054512, 2011.
[8] J. Marczewski, D. Tomaszewski, M. Zaborowski, and P. Bajurko, "Thermoemission-based model of thz detection and its validation-jlfet case studies," *IEEE Trans. Terahertz Sci. Technol.*, vol. 12, no. 6, pp. 633–647, 2022.
[9] F. Ludwig, A. Generalov, J. Holstein, A. Murros, K. Viisanen, M. Prunnila, and H. G. Roskos, "Terahertz detection with graphene fets: Photothermoelectric and resistive self-mixing contributions to the detector response," *ACS Appl. Electron. Mater.*, 2024.

[10] M. A. Andersson and J. Stake, "An accurate empirical model based on volterra series for FET power detectors," *IEEE Trans. Microw. Theory Techn.*, vol. 64, no. 5, pp. 1431–1441, 2016.

[11] X. Yang, A. Vorobiev, K. Jeppson, and J. Stake, "Describing broadband terahertz response of graphene FET detectors by a classical model," *IEEE Trans. Terahertz Sci. Technol.*, vol. 10, no. 2, pp. 158–166, 2019.

[12] M. Bauer *et al.*, "A high-sensitivity AlGaN/GaN HEMT terahertz detector with integrated broadband bow-tie antenna," *IEEE Trans. Terahertz Sci. Technol.*, vol. 9, no. 4, pp. 430–444, 2019.

[13] A. Lisauskas, U. Pfeiffer, E. Öjefors, P. H. Bolìvar, D. Glaab, and H. G. Roskos, "Rational design of high-responsivity detectors of terahertz radiation based on distributed self-mixing in silicon field-effect transistors," *J. Appl. Phys.*, vol. 105, no. 11, 2009.

[14] H. Kojima, D. Kido, H. Kanaya, H. Ishii, T. Maeda, M. Ogura, and T. Asano, "Analysis of square-law detector for high-sensitive detection of terahertz waves," *J. Appl. Phys.*, vol. 125, p. 174506, 2019.

[15] S. Kim, D.-W. Park, K.-Y. Choi, and S.-G. Lee, "MOSFET characteristics for terahertz detector application from on-wafer measurement," *IEEE Trans. Terahertz Sci. Technol.*, vol. 5, no. 6, pp. 1068–1077, 2015.

[16] F. Ludwig, J. Holstein, A. Krysl, A. Lisauskas, and H. G. Roskos, "Modeling of antenna-coupled si mosfets in the terahertz frequency range," *IEEE Trans. Terahertz Sci. Technol.*, 2024 .

[17] G. Dambrine, A. Cappy, F. Heliodore, and E. Playez, "A new method for determining the FET small-signal equivalent circuit," *IEEE Trans. Microw. Theory Techn.*, vol. 36, no. 7, pp. 1151–1159, 1988.

[18] J. Mateos, T. González, D. Pardo, S. Bollaert, T. Parenty, and A. Cappy, "Design optimization of AlInAs-GaInAs HEMTs for high-frequency applications," *IEEE Trans. Electron Devices,*, vol. 51, no. 4, pp. 521–528, 2004.

[19] G. Crupi and D. Schreurs, *Microwave de-embedding: from theory to applications*. Academic Press, 2013.

[20] G. Crupi, A. Caddemi, D. M.-P. Schreurs, and G. Dambrine, "The large world of FET small-signal equivalent circuits," *Int. J. RF Microw. Comput-Aid. Eng.*, vol. 26, no. 9, pp. 749–762, 2016.

[21] G. Paz-Martínez, P. Artillan, J. Mateos, E. Rochefeuille, T. González, and I. Íñiguez-de-la Torre, "A closed-form expression for the frequency dependent microwave responsivity of transistors based on the I-V curve and S-Parameters," *IEEE Trans. Microw. Theory Techn.*, vol. 72, no. 1, pp. 415–420, 2024.

[22] M. I. W. Khan, S. Kim, D.-W. Park, H.-J. Kim, S.-K. Han, and S.-G. Lee, "Nonlinear analysis of nonresonant THz response of MOSFET and implementation of a high-responsivity cross-coupled THz detector," *IEEE Trans. Terahertz Sci. Technol.*, vol. 8, no. 1, pp. 108–120, 2017.

[23] H. Hou, Z. Liu, J. Teng, T. Palacios, and S. Chua, "High temperature terahertz detectors realized by a GaN high electron mobility transistor," *Sci. Rep.*, vol. 7, no. 1, pp. 1–6, 2017.

[24] G. Paz-Martínez, I. Íñiguez-de-la Torre, H. Sánchez-Martín, T. González, and J. Mateos, "Analysis of GaN-based HEMTs operating as RF detectors over a wide temperature range," *IEEE Trans. Microw. Theory Techn.*, vol. 71, no. 7, pp. 3126–3135, 2023.

[25] G. Paz-Martínez, I. Íñiguez-de-la Torre, H. Sánchez-Martín, B. García-Vasallo, N. Wichmann, T. González, and J. Mateos, "Comparison of GaN and InGaAs high electron mobility transistors as zero-bias microwave detectors," *J. Appl. Phys.*, vol. 132, no. 13, p. 134501, 2022.

[26] G. Paz-Martínez, I. Íñiguez-de-la Torre, H. Sánchez-Martín, J. A. Novoa-López, V. Hoel, Y. Cordier, J. Mateos, and T. González, "Temperature and gate-length dependence of subthreshold RF detection in GaN HEMTs," *Sensors*, vol. 22, no. 4, p. 1515, 2022.

[27] G. Paz-Martínez, I. Íñiguez-de-la Torre, P. Artillan, H. Sánchez-Martín, S. García-Sánchez, T. González, and J. Mateos, "High-frequency microwave detection with GaN HEMTs in the subthreshold regime," *IEEE Trans. Microw. Theory Techn.*, pp. 1–0, 2023.

[28] I. Íñiguez-de-la Torre, P. Artillan, G. Paz-Martínez, E. Rochefeuille, T. González, and J. Mateos, "Responsivity measurements up to 110 GHz using AlGaN/GaN HEMTs with different gate size," in *2023 International Workshop on Integrated Nonlinear Microwave and Millimetre-Wave Circuits (INMMIC)*, 2023, pp. 1–3.

[29] P. Altuntas *et al.*, "Power performance at 40 GHz of AlGaN/GaN high-electron mobility transistors grown by molecular beam epitaxy on Si (111) substrate," *IEEE Electron Device Lett.*, vol. 36, no. 4, pp. 303–305, 2015.

[30] S. Rennesson *et al.*, "Optimization of $\mathrm{Al_{0.29}Ga_{0.71}N/GaN}$ high electron mobility heterostructures for High-Power/Frequency performances," *IEEE Trans. Electron Devices*, vol. 60, no. 10, pp. 3105–3111, 2013 .

[31] S. D. Nsele, L. Escotte, J.-G. Tartarin, S. Piotrowicz, and S. L. Delage, "Broadband frequency dispersion small-signal modeling of the output conductance and transconductance in AlInN/GaN HEMTs," *IEEE Trans. Electron Devices*, vol. 60, no. 4, pp. 1372–1378, 2013 .

[32] M. Malmkvist, S. Wang, and J. V. Grahn, "Epitaxial optimization of 130-nm gate-length InGaAs/InAlAs/InP HEMTs for high-frequency applications," *IEEE Trans. Electron Devices,*, vol. 55, no. 1, pp. 268–275, 2007 .

[33] B. J. Touchaei and M. Shalchian, "A compact Non-Quasi-Static small-signal model for GaN HEMT," *Microelectronics Journal*, vol. 148, p. 106199, 2024.